International Journal of Biological Macromolecules 367 (2026) 152550

Contents lists available at ScienceDirect

International Journal of Biological Macromolecules

journal homepage: www.elsevier.com/locate/ijbiomac

Unlocking the skin protection potential of discarded *Dictyophora rubrovalvata* volva: Structural, rheology and anti-photoaging insights into its unique polysaccharides

Ziwei Li [a,b,1], Peng Liu [a,1], Di Wu [a], Zhong Zhang [a], Wanchao Chen [a], Wen Li [a], Yuanfeng Wang [b], Yan Yang [a,*]

[a] *Institute of Edible Fungi, Shanghai Academy of Agricultural Sciences, National Engineering Research Center of Edible Fungi, Key Laboratory of Edible Fungi Resources and Utilization (South), Ministry of Agriculture, 201403, China*
[b] *College of Life Sciences, Shanghai Normal University, 201418, China*

ARTICLE INFO

Keywords:
Dictyophora rubrovalvata
Discarded volva polysaccharides
Rheological properties
Skin photoaging

ABSTRACT

Dictyophora rubrovalvata is a valuable edible fungus, while research on its bioactive components has primarily focused on the fruiting body, other parts, notably the discarded volva colloid, remain underexplored. In order to explore the skin protection of polysaccharides from volva colloid, herein, polysaccharides from the fruiting body (IP), pileus (FP), and volva colloid (VP) were extracted. Rheological assessment indicated pseudoplastic behavior for all three polysaccharides, while VP showed the fastest recovery to its original state, displaying weak gel property and sol-gel transition ability. Furthermore, IP, FP and VP effectively mitigated UVB-induced cytotoxicity in human skin fibroblasts (HSFs). All polysaccharides significantly enhanced cellular antioxidant capacity, evidenced by elevated levels of SOD, CAT, and GSH-Px, alongside reduced MDA and ROS production. Notably, VP conferred the strongest protection against UVB-induced skin photoaging. RNA-sequencing analysis implicated the regulatory role of VP in the TNF pathway as a key mechanism underlying this superior photoprotection. The unique properties and bioactivities of *D. rubrovalvata* discarded volva polysaccharides provide a basis for the development of *D. rubrovalvata* waste.

1. Introduction

Skin photoaging refers to the premature aging of skin structures resulting from chronic exposure to ultraviolet (UV) radiation, driven primarily by alterations in cellular metabolism and oxidative stress due to changes in enzymatic activities [1–3]. Additional contributing factors include inflammation, disruption of skin barrier homeostasis, collagen denaturation, and abnormal pigmentation [4]. It is widely recognized that reactive oxygen species (ROS) generated by UV radiation act as a unifying pathogenic element in these processes [5]. ROS can deplete the skin's endogenous antioxidant defense systems and activate signaling pathways associated with cell growth, differentiation, senescence, and degradation of the extracellular matrix in dermal fibroblasts [5–7]. The adverse effects of photoaging (such as telangiectasia, dyspigmentation, skin dryness, laxity, wrinkle formation, and even precancerous lesions) have spurred growing demand for effective interventions. Unfortunately, no pharmaceutical agents have yet been developed that fully counteract UVA-induced photoaging [8]. In recent years, various natural bioactive compounds have shown promise in the prevention and treatment of skin photoaging with fewer adverse effects. Examples include tea polyphenols [9], marine-derived bioactive peptides [10], seaweed extracts [11], and polysaccharides. For example, *dendrobium officinale* polysaccharides could achieve photoaging protection by inhibiting oxidative stress, alleviating cell cycle arrest and apoptosis [12]. *Inonotus obliquus* polysaccharides inhibited oxidative stress-induced premature aging and DNA damage, and promoted skin health [13]. However, the widespread application of such natural products is often limited by high production costs. Thus, there is an urgent need to identify low-cost, naturally derived active ingredients that can effectively support skin health.

Dictyophora rubrovalvata is characterized by its distinctive structure, which includes a spongy stipe, a bell-shaped pileus, and a delicate net-

* Corresponding author.
E-mail address: yangyan@saas.sh.cn (Y. Yang).
[1] co-first author

https://doi.org/10.1016/j.ijbiomac.2026.152550
Received 23 July 2025; Received in revised form 11 May 2026; Accepted 13 May 2026
Available online 14 May 2026

like skirt. During its developmental stages, the fungus is enclosed within a gelatinous, egg-like volva, which is typically discarded upon maturation of the fruiting body, leading to significant resource wastage. Despite this, *D. rubrovalvata* has attracted attention for its nutritional and medicinal value [14–16]. These polysaccharides from the *D. rubrovalvata* fruiting body can effectively improve intracellular nucleic acid and glycogen metabolism [17]. Huang et al. [18] indicated that *D. rubrovalvata* polysaccharides possessed immunoactivity by balancing the excessive inflammation, and molecular weight is an important factor affecting immunoactivity. However, most investigations have focused exclusively on polysaccharides from the fruiting body, while those from the pileus and the volva (often considered agricultural waste) remain poorly studied. In particular, systematic research on the physicochemical and structural properties of polysaccharides derived from the volva of *D. rubrovalvata* is still lacking.

Accordingly, this study aims to explore the structural characteristics and anti-photoaging activities of polysaccharides extracted from different parts (including pileus, fruiting body, and volva colloid) of *D. rubrovalvata*, with a specific focus on the underutilized volva. Furthermore, we investigated the potential mechanism by which volva-derived polysaccharides exert their anti-aging effects. This work provides a scientific foundation for the value-added utilization of *D. rubrovalvata* by-products.

2. Materials and methods

2.1. Materials

D. rubrovalvata was obtained from Shanghai Guosen Biotechnology Co., Ltd. (Shanghai, China). Human skin fibroblast (HSF) cell line was purchased from Sinopharm Chemical Reagent Co., Ltd. (Shanghai, China). Glucose, glucuronic acid, anhydrous ethanol, trifluoroacetic acid, and phosphate-buffered saline (PBS) were supplied by Sinopharm Group Co., Ltd. DMEM medium, trypsin, and fetal bovine serum (FBS) were obtained from GIBCO (Carlsbad, USA). Superoxide dismutase (SOD) assay kit, catalase (CAT) assay kit, glutathione peroxidase (GSH-Px) assay kit, and malondialdehyde (MDA) assay kit were purchased from Nanjing Jiancheng Bioengineering Institute (Nanjing, China). All other chemicals and reagents used were of analytical grade.

2.2. Preparation of polysaccharides from different parts of D. Rubrovalvata

The mature *D. rubrovalvata* was separated into three parts: fruiting body, pileus, and volva. The fruiting body and pileus were dried and pulverized to obtain fruiting body powder and pileus powder. These powders were mixed with distilled water at a solid-to-liquid ratio of 1:10 (*w/v*) and subjected to hot water extraction. The mixture was heated to 100 °C with continuous stirring for 2 h, followed by centrifugation at 8000 rpm for 20 min to collect the supernatant. For the volva, the purple outer skin and white inner membrane were removed to collect the inner colloid layer. The colloid was homogenized using a blender for 3–5 min and centrifuged at 8000 rpm for 20 min to collect the supernatant. The supernatants from the fruiting body, pileus, and volva were precipitated overnight at 4 °C using 50% ethanol. The resulting precipitates were centrifuged, washed three times with ethanol, and freeze-dried to obtain the polysaccharides from the fruiting body (IP), pileus (FP), and volva colloid (VP), respectively.

2.3. Determination the content of composition

The polysaccharide content was determined using the phenol-sulfuric acid method [20]. The glucuronic acid content was measured using the sulfuric acid-carbazole method [21], and the protein content was quantified using the BCA assay kit.

2.4. Analysis of structural characteristics

2.4.1. Monosaccharide composition analysis

Based on a modified method from the reference [22, 23], 2 mg of the sample was placed in a pear-shaped flask and hydrolyzed with 3 mL of 2 mol/L trifluoroacetic acid (TFA) at 110 °C for 4 h. The monosaccharide composition and molar ratio of the hydrolysis products were analyzed using high-performance anion-exchange chromatography (HPAEC).

2.4.2. Fourier transform infrared (FT-IR) spectroscopy analysis

2.0 mg of freeze-dried sample was scanned using an FT-IR spectrometer. The spectra were collected in the range of 500–4000 cm^{-1} with a resolution of 4 cm^{-1} and 64 scans [24].

2.4.3. Scanning Electron microscopy (SEM)

1 mg of crude polysaccharide from different parts of *D. rubrovalvata* was used for SEM analysis. The samples were gold-coated for 15 min and observed under an acceleration voltage of 0.5–30 kV at magnifications of 500× to examine their microstructures [25].

2.5. In vitro antioxidant activity

The scavenging capacity of DPPH radicals was determined based on the method reported by Mtetwa et al. [26], with slight modifications. 0.1 mM DPPH solution was prepared and stored in the dark. Two sets of sample solutions with different concentrations were prepared: a sample group and a control group. The sample group was mixed with 1 mL of DPPH solution, the control group with 1 mL of absolute ethanol, and the blank group with 1 mL of distilled water instead of the sample solution, followed by the addition of 1 mL of DPPH solution. The mixtures were incubated in the dark at room temperature for 30 min, and the absorbance was measured at 517 nm.

The 2,2′-azinobis-(3-ethylbenzothiazoline-6-sulfonate) (ABTS) radical scavenging capacity was evaluated following the method reported [27], with slight modifications. A solution was prepared by mixing 5 mL ABTS (7 mM) and 5 mL potassium persulfate (2.45 mM), then the mixture was stood in the dark for 12 h. After that the mixture was diluted with pH 6.6 phosphate buffer to achieve an absorbance of 0.7 at 734 nm (ABTS solution). 0.2 mL sample solution was mixed with 2 mL of the ABTS solution and allowed to react in the dark for 6 min. The absorbance was measured at 734 nm.

2.6. Evaluation of rheological properties

The rheological properties of IP, FP, and VP were analyzed using a rheometer at 25 °C based on the previously reported method [28], with slight modifications. A cone-plate geometry (PP50) with a gap of 0.1 mm was employed.

2.6.1. Steady-state rheology

The steady-state flow behavior of IP, FP, and VP was evaluated at concentrations of 5 mg/mL and 10 mg/mL under a shear rate ranging from 0.1 to 1000 s^{-1} [29]. The data were fitted to the power-law model to describe the flow behavior:

$$\tau = K\,\gamma n$$

where τ is the shear stress (Pa), γ is the shear rate (s^{-1}), K is the consistency coefficient ($Pa{\cdot}s^n$), and nis the flow behavior index.

2.6.2. Viscoelastic behavior

To investigate dynamic oscillatory frequency scanning, IP, FP, and VP at different concentrations (5 and 10 mg/mL) were prepared and measured under 1% strain across a frequency range of 1–100 rad/s [30].

2.6.3. Thixotropy

The shear rate was first increased from 0.1 s^{-1} to 100 s^{-1} and then immediately decreased back to 0.1 s^{-1} at the same rate. During this process, the shear stress of each sample solution was recorded to fit the upward and downward flow curves. The thixotropic properties of IP, FP, and VP solutions at a concentration of 5 mg/mL were examined. The following formula is used to calculate the area of the hysteresis loop [31]:

$$\text{Hysteresis loop area} = \int_{\gamma 2}^{\gamma 1} k1(\gamma)^{n1} - \int_{\gamma 2}^{\gamma 1} k2(\gamma)^{n2.}$$

Where γ_1 and γ_2 represent the initial and final shear rates, $k_1$and k_2 are the consistency coefficients of the upward and downward curves, and n_1 and n_2 are the flow behavior indices of the upward and downward curves, respectively.

2.7. Evaluation of the effects on UVB-induced skin Photodamage

2.7.1. Cell viability

Cell viability of HSF cells was assessed using an MTT assay [32]. HSF cells in the logarithmic growth phase were seeded into 96-well plates at a density of 1×10^4 cells per well, with 180 μL of medium added to each well. The plates were incubated at 37 °C in a humidified atmosphere containing 5% CO_2 for 24 h. After incubation, the supernatant was discarded, and the cells were washed twice with PBS. Subsequently, 20 μL of different sample concentrations (final concentrations of 5, 10, 25, 50, 100, 200 and 400 μg/mL) were added to the corresponding wells. PBS (20 μL) was added to the control group. After 48 h of treatment, 20 μL of MTT solution (5 mg/mL) was added to each well, and the plates were incubated for an additional 4 h. The reaction was terminated by carefully removing the medium, and 150 μL of dimethyl sulfoxide (DMSO) was added. The absorbance of each well was measured at 490 nm using a microplate reader.

2.7.2. Protective effects against UVB-induced skin Photodamage in HSF cells

Establishment of the UVB-induced skin photodamage model: HSF cells were cultured for 24 h following the procedure described in 2.7.1. After incubation, the medium was discarded, and added 50 μL of PBS to each well. A UV radiation meter was used to measure the radiation intensity of a UVB lamp (4 W, primary wavelengths ranging from 280 nm to 320 nm, with a peak at 308 nm) positioned 10 cm from the radiation surface [33]. The UVB exposure doses were calculated using the following formula:

$$\text{UVB Dose}\left(\text{mJ}/\text{cm}^2\right) = \text{Radiation Intensity}(\text{mW}/\text{cm2}) \times \text{Exposure Time}(\text{s})$$

Exposure doses were set at 0, 10, 20, 40, 60, and 80 mJ/cm^2. Six replicates were prepared for each dose. During the irradiation of each group with a specific UVB dose in the 96-well plates, aluminum foil was used to cover the other groups to avoid cross-group variability. After UVB exposure, the PBS was discarded, and complete medium was added to the wells, followed by incubation for 24 h. The cell viability was calculated.

HSF cells were cultured for 24 h, 20 μL IP, FP, and VP at different concentrations (100, 200, and 400 μg/mL) were added to the cells. In the control (CON) group and the model (UV) group, 20 μL PBS was added. The cells were then incubated for another 24 h. After incubation, the culture medium was discarded, and cells in all groups were subjected to UVB irradiation at a dose of 40 mJ/cm^2. Following irradiation, the PBS was discarded, and complete culture medium was re-added to the wells. The cells were further incubated for 24 h, and then the cell viability was determined.

2.7.3. Detection of ROS level

HSF cells were seeded into 24-well plates at a density of 1×10^5 cells/well and cultured for 24 h. After discarding the supernatant, the treatment groups received IP, FP, and VP at different concentrations (100, 200, and 400 μg/mL), while the control group and the model group were treated with PBS. All groups were incubated for another 24 h. Following incubation, cells were irradiated with UVB at a dose of 40 mJ/cm^2. After irradiation, the PBS was removed, and complete culture medium was re-added. The cells were then incubated for another 24 h. At the end of the incubation, the culture medium was replaced with DMEM containing 10 μM DCFH-DA. After a 20 min incubation, the fluorescence intensity within cells was quantified using flow cytometry. Fluorescence images of the cells were also captured using a fluorescence microscope [34].

2.7.4. Analysis of oxidative stress enzyme activities

The protein concentration was determined using a protein quantification assay kit. The activities of SOD (superoxide dismutase), CAT (catalase), and GSH-Px (glutathione peroxidase), as well as the MDA (malondialdehyde) content, were measured according to the corresponding kit instructions.

2.8. RNA-seq analysis

HSF cells with different treatments were collected, including cells in the control group (C), model group (M) and 400 μg/mL VP-treated group (VP). Total RNA was extracted from collected cell samples using the Trizol method [35]. Agilent 2100 and Nanodrop were used to determine RNA quality. After enriching the mRNA using magnetic beads and Oligo (dT), short fragments of the mRNA were created by adding fragmentation buffer. Random hexamers were used for reverse transcription, and buffer, dNTPs, and DNA polymerase I were added to create two-stranded cDNA. After a series of purifications, repair, and amplification, the cDNA library was constructed. Using the Illumina high-throughput sequencing platform (HiSeqTM2500), the prepared libraries were sequenced using the PE150 strategy and then compared to the reference genome sequence using STAR (v2.5.2b). HTSeq software was used to analyze the gene expression levels of each sample to obtain FPKM (Fragments per kilobase of exon model per million mapped reads) values. Next, DESeq was used to determine the differentially expressed genes based on $|\log_2(\text{FoldChange})| > 1$ and p value <0.05. GOSEq. (v1.22) and KOBAS (v2.0) were used to perform differential gene GO enrichment and KEGG enrichment analysis on the corrected p-value<0.05.

2.9. Statistical analysis

All experiments were performed at least three times, and data are presented as mean ± standard deviation (SD). Statistical significance between groups was analyzed using SPSS 26.0, with a P-value of <0.05 considered significant. Graphs were generated using Origin 2023 software. Volcano plots were created using R language, and Venn diagrams were plotted using the Venny2.1 online tool.

3. Results

3.1. Monosaccharide composition

In this study, polysaccharides were extracted from three distinct parts of *D. rubrovalvata,* including the stipe (IP), pileus (FP) and volva colloid (VP) (Fig. 1A). The polydispersity index (*Mw/Mn*) used to evaluate molecular weight distribution [36], ranged from 1.26 to 1.58 across the samples. Monosaccharide composition analysis indicated that all three polysaccharide fractions consisted of fucose, galactose, glucose, mannose, and glucuronic acid. Glucose was the predominant monosaccharide in both IP and FP, whereas VP was characterized by high proportions of glucose and glucuronic acid. In addition, all samples

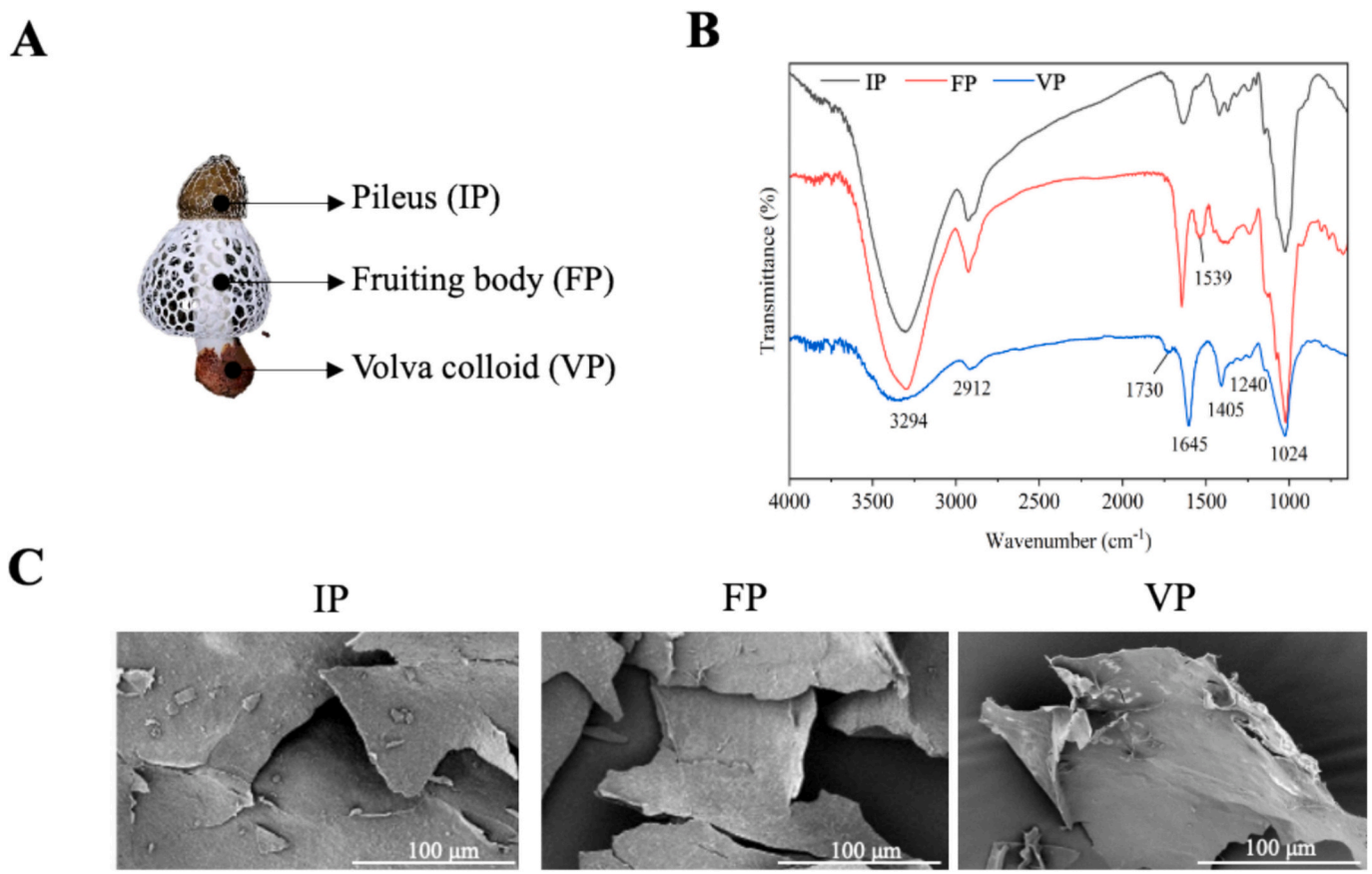

Fig. 1. Characterization of IP, FP and VP. (A). IP, FP and VP were extracted from the three different parts of *D. rubrovalvata* (B). FT-IR spectra and (C) SEM images of IP, FP and VP.

contained low levels of protein, with IP, FP, and VP being 4.4%, 8.9%, and 10.8%, respectively. Notably, the composition of VP differed considerably from that of the stipe and pileus polysaccharides. While previous studies have reported the presence of arabinose in stipe-derived polysaccharides of *D. rubrovalvata* [37], none was detected in the present extracts, a discrepancy that may be attributed to variations in cultivation conditions or raw material sources [38]. The distinct chemical profiles observed here, particularly the high glucuronic acid content in VP, suggest that polysaccharides from different parts of *D. rubrovalvata* may exhibit divergent bioactivities. This inference is consistent with earlier findings by Aremu et al. [39], which highlighted the influence of chemical composition on the pharmacological properties of natural products.

3.2. Microstructure characteristics

3.2.1. Fourier transform infrared (FT-IR) spectroscopy analysis

The FT-IR spectra of IP, FP, and VP were showed in Fig. 1B. The three polysaccharides exhibited similar absorption profiles characteristic of common functional groups. A broad and intense peak around 3294 cm^{-1} was assigned to O—H stretching vibrations [40], while the signal at 2912 cm^{-1} corresponded to C—H stretching in methyl groups [41]. Additional characteristic peaks included the C═O stretching vibration at 1645 cm^{-1}, along with absorptions at 1405 cm^{-1} and 1240 cm^{-1}, attributed to carboxyl group (–COOH) stretching and C—O vibrations, respectively [28]. A notable peak at 1024 cm^{-1} was associated with the asymmetric stretching of D-pyranose rings and absorption from lactone and hydroxyl groups within the pyranose structure, consistent with typical glucan-related FT-IR features [42]. Despite these shared spectral characteristics, distinct differences were observed among the polysaccharides. FP displayed a unique absorption peak at 1539 cm^{-1}, commonly linked to C═C stretching vibrations [43]. More notably, VP exhibited a characteristic peak at 1730 cm^{-1}, indicative of esterified carboxyl groups (–COOR) [44]. This finding is consistent with the higher uronic acid content previously identified in VP, supporting its distinct structural properties.

3.2.2. Scanning electron microscopy (SEM)

The SEM images of IP, FP, and VP were presented (Fig. 1C). The results revealed that polysaccharides from different parts of *D. rubrovalvata* exhibited a sheet-like distribution with dispersed structures, resembling the morphology of other natural polysaccharides reported in previous studies [45]. The polysaccharide fragments of IP and FP appeared larger than those of VP, while the surface of VP polysaccharides was rough and dense, with small porous structures. These pores provided a structural basis for the good water- and oil-holding capacities of polysaccharides [46]. In contrast, the surfaces of IP and FP polysaccharides were smoother and denser, with IP exhibiting the most compact surface.

3.3. Rheological properties

3.3.1. Steady-state rheology

The steady-state rheological properties of polysaccharides from different parts of *D. rubrovalvata* were evaluated. The high R^2 values (>0.96) for all samples confirmed the suitability of the applied model for characterizing their flow behavior (Table 1). As the polysaccharide concentration increased from 5 to 10 mg/mL, the consistency index (K) rose, likely due to enhanced molecular entanglement and intermolecular interactions [48]. All samples exhibited flow behavior indices (*n*) below 1, ranging from 0.168 to 0.364, confirming pseudoplastic characteristics [49]. Lower *n* values indicate more pronounced pseudoplastic behavior

Table 1
The apparent viscosity (shear stress-shear rate) test was fitted by the power-law model.

Concentration (mg/mL)	Sample	Consistency coefficient (K)	Flow index (n)	determination coefficients (R^2)
5	IP	1.154 ± 0.049	0.266 ± 0.008	0.965
	FP	0.109 ± 0.002	0.363 ± 0.004	0.996
	VP	0.164 ± 0.002	0.364 ± 0.003	0.998
10	IP	5.529 ± 0.113	0.168 ± 0.004	0.970
	FP	0.317 ± 0.006	0.276 ± 0.006	0.985
	VP	0.865 ± 0.008	0.219 ± 0.003	0.994

[50]. Consistent with these findings, the apparent viscosity of IP, FP, and VP decreased with increasing shear rate (Fig. 2A, B), a hallmark of shear-thinning fluids [51]. This behavior arises from the disruption of intermolecular associations (such as hydrogen bonds and van der Waals forces) under shear stress, leading to the breakdown of aggregated structures and a consequent drop in viscosity [28]. The shear-thinning response was concentration-dependent, with more pronounced effects at higher polysaccharide concentrations. In concentrated solutions, polysaccharide chains form a dynamic entangled network. While shearing disrupts existing entanglements, new interactions rapidly form, maintaining structural integrity [52], at higher concentrations, chain mobility becomes restricted, increasing interaction density and enhancing consistency and pseudoplasticity [53]. Moreover, the different flow states can be clearly observed here, especially the molecular chains of IP were highly entangled at higher concentrations and were difficult to untie under shear, due to its high molecular weight. The dense network structure formed by entanglement significantly increases the viscosity of the solution, leading to an increase in molecular diffusion resistance. Comparatively, VP and FP exhibited more advantages in crossing the skin penetration barrier.

3.3.2. *Viscoelastic behavior*

The viscoelastic behavior of polysaccharide solutions from *D. rubrovalvata* was characterized by monitoring the storage modulus (G′) and loss modulus (G″) as functions of angular frequency (ω) [54]. As

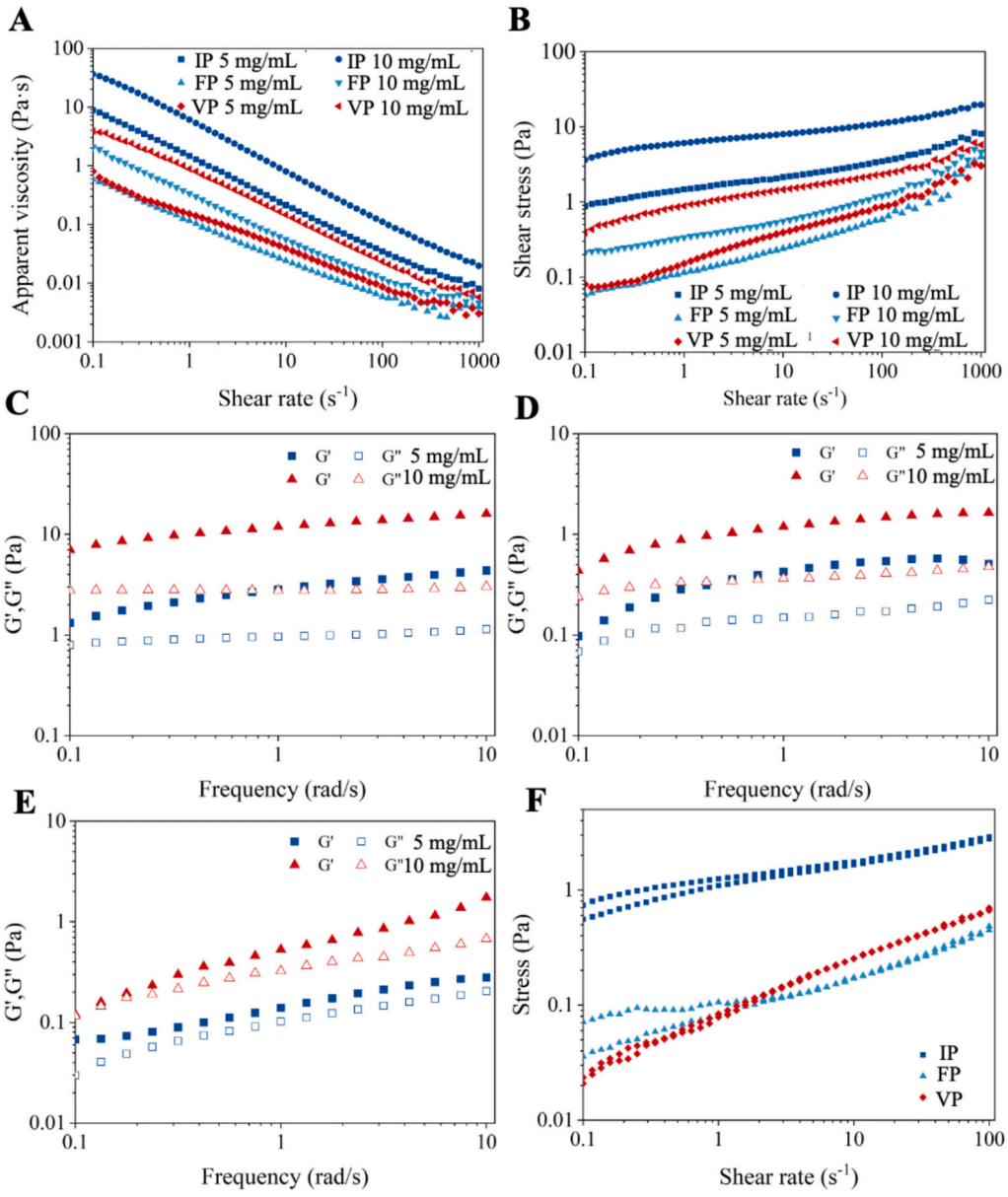

Fig. 2. Rheological properties. (A) Apparent viscosity, (B) shear stress, (C-E) viscoelastic behavior and (F) thixotropic behavior of IP, FP and VP at different concentrations (5 and 10 mg/mL) at 25 °C.

shown in Fig. 2C–E, both moduli increased with frequency for IP, FP, and VP. This rise in G′ reflects enhanced structural integrity, attributable to an increased number and size of junction zones, indicating strong deformation resistance in these polysaccharides [55]. Across the tested concentrations (5 and 10 mg/mL), G′ consistently exceeded G″ in all samples, demonstrating solid-like, elastic-dominated mechanical responses [56]. IP, FP, and VP exhibited typical polymer concentration dependence. Within the frequency range of 0.1–10 rad/s, IP and FP showed minimal frequency dependence—a behavior consistent with rigid hydrogel networks having limited chain mobility [57]. It was reported that in strong or real gel, also $G' > G''$, but the slope of the curves of G′ and G″ moduli was almost zero, and not dependent on frequency [58]. In contrast, VP at 10 mg/mL displayed a crossover point between G′ and G″ in the low-frequency region, indicating a transition from liquid-like to gel-like behavior beyond a critical frequency. Both moduli of VP increased markedly with frequency across concentrations, supporting its classification as a weak gel with substantial elastic character and the ability to form a cohesive network through interchain associations [59]. Consequently, IP and FP possessed a rigid solid gel network, facing diffusion and absorption constraints and poor ductility. While VP exhibited a crosslinked viscoelastic gel network, which had shear thinning characteristics and was more conducive to transdermal absorption.

3.3.3. Thixotropy behavior

The thixotropic behavior of polysaccharides, reflected by the hysteresis loop formed between the ascending and descending shear stress curves [60], indicates the extent of structural breakdown and recovery under shear [61]. A larger hysteresis area corresponds to stronger thixotropy and slower structural regeneration. In this study, the thixotropic properties of 5 mg/mL IP, FP, and VP were evaluated (Fig. 2F). The measured hysteresis loop areas were 10.386 ± 0.093 Pa/s for IP, 1.457 ± 0.042 Pa/s for FP, and 1.118 ± 0.013 Pa/s for VP. VP exhibited the smallest hysteresis area, indicating that its gel-like structure undergoes rapid recovery after shear deformation [62]. In contrast, IP and FP formed denser and more persistent networks, as evidenced by their larger hysteresis areas, yet showed slower structural regeneration. These results confirm that VP possesses weak gel characteristics and reversible sol–gel transition behavior, suggesting its superior suitability for topical skin protection applications.

3.4. Protective effect against skin photodamage

3.4.1. Enhancement of cell viability of HSF cells induced by UVB irradiation

Ultraviolet B (UVB) radiation is a major environmental factor responsible for skin inflammation, premature aging, and carcinogenesis [63]. To evaluate the photoprotective potential of IP, FP, and VP, a cellular model of skin photodamage was established by exposing human hypertrophic scar fibroblasts (HSFs) to UVB irradiation (0–80 mJ/cm^2). As illustrated in Fig. 3A, cell viability declined progressively with increasing UVB doses. A dose of 40 mJ/cm^2 was selected for subsequent experiments, as it reduced cell viability to 57.53%, representing a substantial yet sublethal injury suitable for assessing protective effects.

Prior to photoprotection assays, cytotoxicity of the polysaccharides was assessed. Treatment with IP, FP, and VP at concentrations up to 400 μg/mL did not significantly impair HSF viability (all >80%, Fig. 3B), supporting their biocompatibility. Thus, concentrations of 100, 200, and 400 μg/mL were chosen for further study. As shown in Fig. 3C, UVB exposure markedly decreased the viability of HSFs in the model group compared to the untreated control. However, pretreatment with IP, FP, or VP significantly attenuated this UVB-induced loss of cell viability in a dose-dependent manner. Notably, VP demonstrated superior protective efficacy compared to IP and FP, suggesting its enhanced potential in mitigating UVB-induced photodamage.

3.4.2. Amelioration of oxidative stress

3.4.2.1. Reduction of ROS level in HSF cells. The oxidative stress theory is widely recognized as a key mechanism in skin photoaging [64]. UVB irradiation disrupts the balance between reactive oxygen species (ROS) production and elimination, leading to oxidative damage that affects nucleic acids, proteins, and lipids, ultimately impairing cellular metabolism and skin function [65–68]. In this study, we first evaluated intracellular ROS levels in HSF cells following UVB exposure. As shown in Fig. 4A, UVB irradiation significantly increased ROS generation, whereas treatment with IP, FP, or VP effectively suppressed this increase, demonstrating the antioxidant capacity of these *D. rubrovalvata* polysaccharides. All three polysaccharides reduced ROS levels in a dose-dependent manner, with VP exhibiting the strongest effect across all concentrations tested, followed by FP. Previous studies have indicated that polysaccharides with lower molecular weights, such as hyaluronic acid and fucoidan, often show enhanced efficacy in mitigating skin photodamage [69,70]. Given that VP possesses a lower molecular weight compared to IP and FP, its superior ROS-scavenging ability may be attributed, at least in part, to this structural characteristic.

3.4.2.2. Enhancement of the enzymatic antioxidant defense system capacity in HSF cells. The intracellular redox balance is maintained by enzymatic antioxidants such as GSH-Px, CAT, and SOD, which collectively neutralize free radicals and ROS to mitigate oxidative damage [71]. As shown in Fig. 4B–E, UVB irradiation significantly reduced the activities of SOD, CAT, and GSH-Px in HSF cells, while elevating MDA levels,

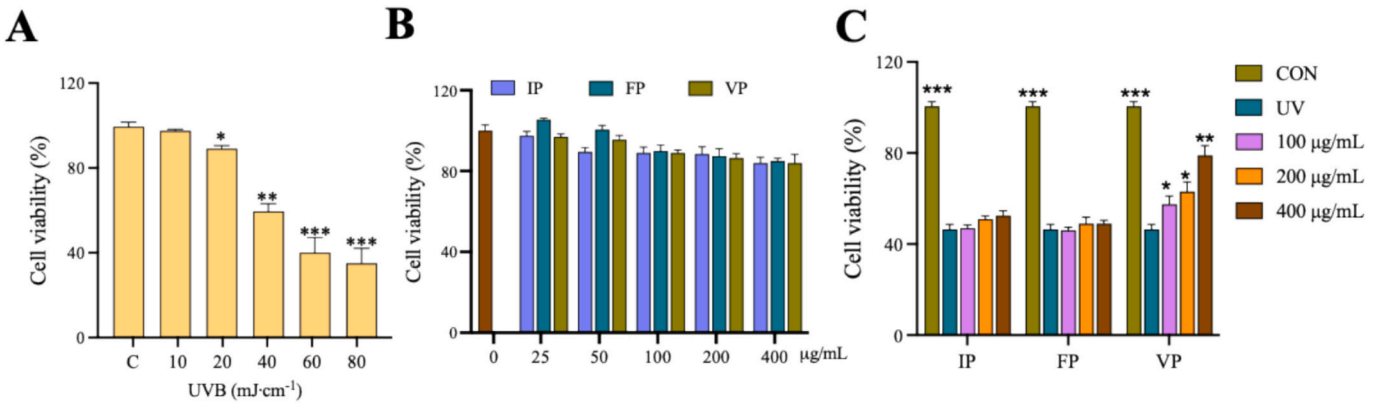

Fig. 3. IP, FP and VP enhanced cell viability of HSF cells induced by UVB irradiation. Skin photodamage model induced by UVB was established (A). The toxic effects of different concentrations of IP, FP and VP on HSF (B), and the effects of IP, FP and VP on the activity of HSF damaged by ultraviolet (UVB). All values are presented as means ± SD ($n = 3$), there is a statistically significant difference between the other groups and UV group (*: $p < 0.05$, **: $p < 0.01$, ***: $p < 0.001$).

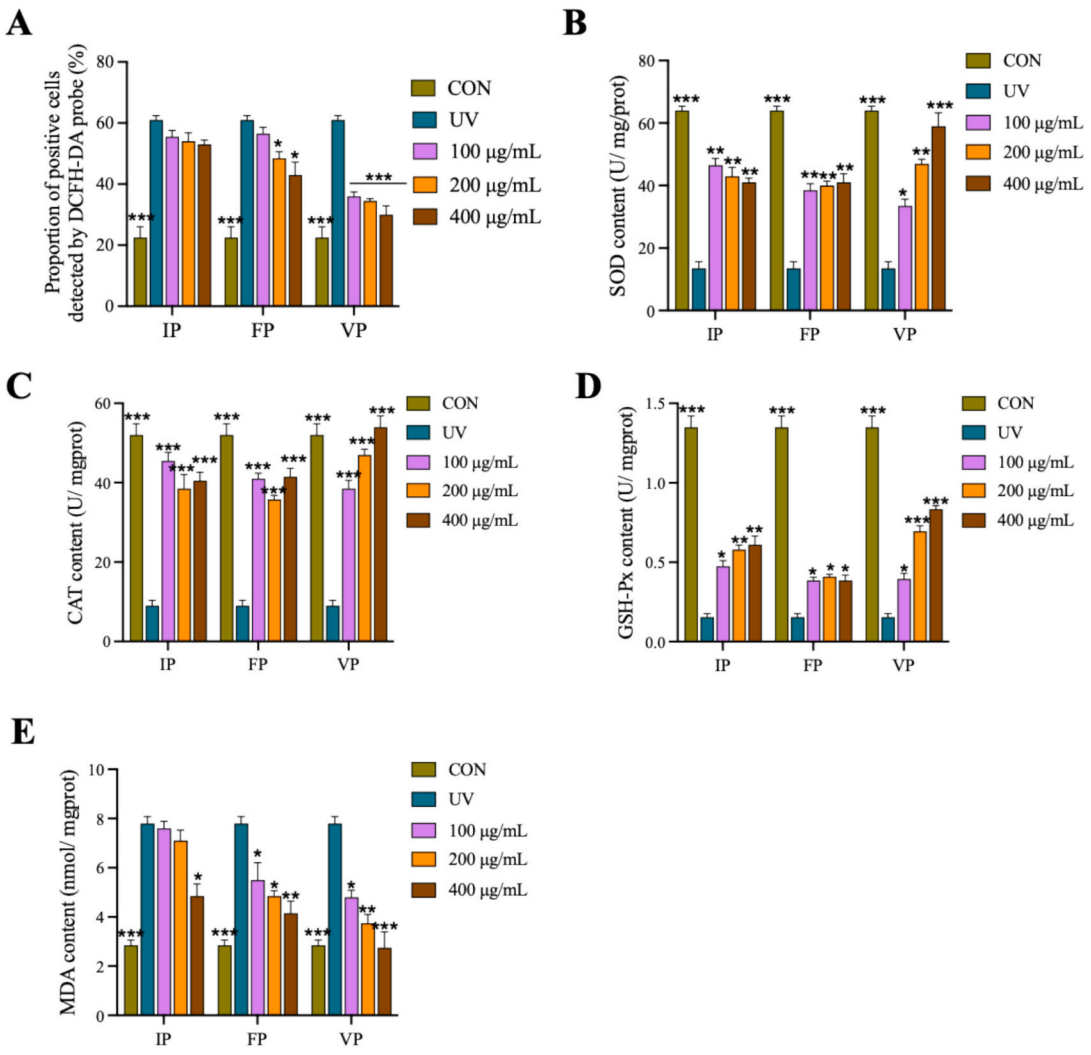

Fig. 4. IP, FP and VP reduced ROS and enhanced antioxidant enzyme level in HSF cells. The ROS level (A) in HSF cells were detected (200 ×). The activities of SOD (B), CAT (C), GSH-Px (D) and MDA(E) in HSF cells were explored. All values are presented as means ± SD ($n = 3$), there is a statistically significant difference between the other groups and UV group (*: $p < 0.05$, **: $p < 0.01$, ***: $p < 0.001$).

indicative of oxidative stress. Treatment with IP and FP restored SOD activity to varying degrees, with VP demonstrating a dose-dependent enhancement. At 400 μg/mL, VP restored SOD activity to a level comparable to that of the non-irradiated control. CAT activity was also ameliorated by polysaccharide treatment. While IP and FP showed the highest restoration at 100 μg/mL, VP exerted a dose-dependent protective effect on CAT activity, outperforming the other two extracts in counteracting UVB-induced suppression. Similarly, VP treatment

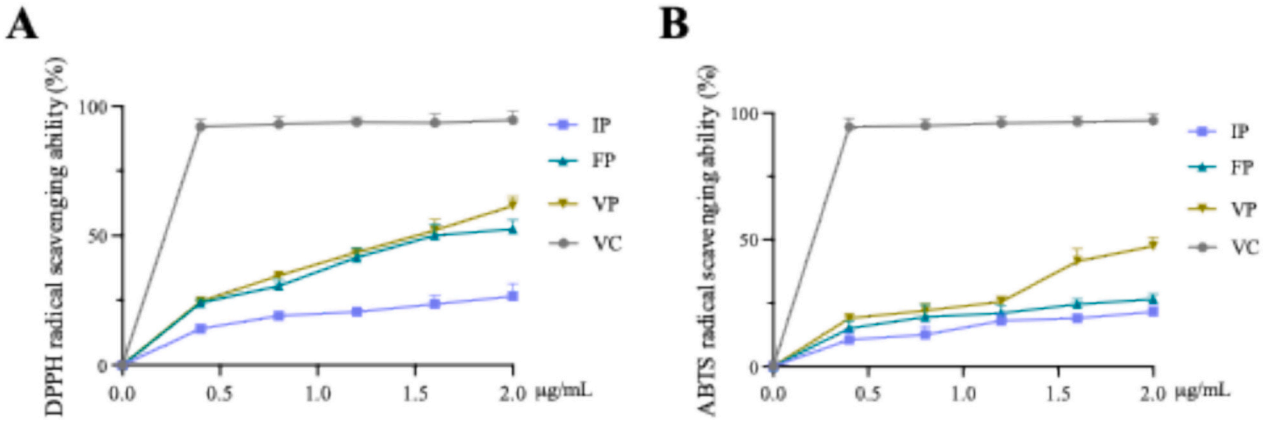

Fig. 5. *In vitro* antioxidant activities of IP, FP, and VP. (A) DPPH radical scavenging activity and (B) ABTS radical scavenging activity. All values are presented as means ± SD ($n = 3$).

resulted in a dose-dependent recovery of GSH-Px activity. In addition, both IP and VP reduced MDA accumulation in a concentration-dependent manner. Consequently, IP, FP and VP possessed excellent ability to improve skin antioxidant capacity, and VP exhibited better protective potential against UVB- induced skin photodamage.

3.4.2.3. Increase of the radical scavenging activities. The *in vitro* antioxidant activities of IP, FP, and VP were evaluated using DPPH and ABTS radical scavenging assays. As depicted in Fig. 5A, all three polysaccharides scavenged DPPH radicals in a dose-dependent manner, with VP showing the highest activity, followed by FP and IP. A similar dose-dependent trend was observed in the ABTS assay (Fig. 5B). Notably, all samples exhibited stronger scavenging effects against DPPH than ABTS radicals, which may reflect differences in the underlying radical-quenching mechanisms and the sensitivity of the assay systems employed [72]. Among the samples, VP demonstrated the most potent ABTS radical scavenging capacity. Antioxidant performance in polysaccharides is known to be influenced by structural features such as glucuronic acid content, molecular weight, monosaccharide composition, and glycosidic linkage patterns [73,74]. The superior antioxidant activity of VP observed in both assays is likely attributable to its higher glucuronic acid content. This aligns with existing literature indicating that elevated glucuronic acid levels enhance the bioactivity of polysaccharides, thereby supporting the consistency and relevance of our findings.

3.5. The alleviate mechanism of UVB-induced skin photodamage

3.5.1. Differential gene expression analysis

Building on the observed photoprotective effects of *D. rubrovalvata* volva polysaccharide (VP) against UVB-induced skin injury, we performed RNA-seq to investigate the underlying molecular mechanisms.

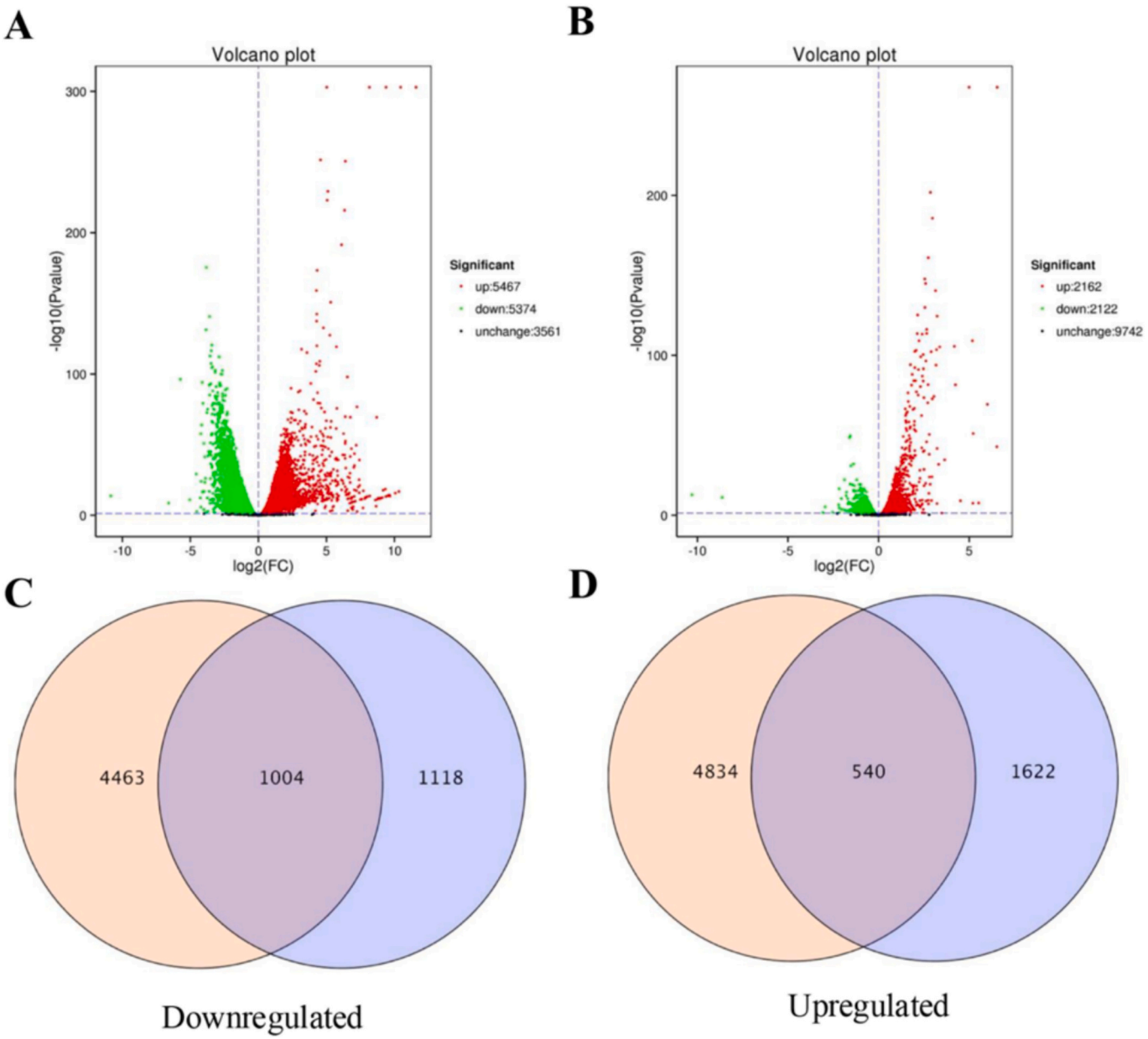

Fig. 6. Differential genes regulated by VP were screened. Compared with the C group, the number of differentially expressed genes (DEGs) induced by UVB was showed (A). Compared with the M group, the number of DEGs treated by VP was showed (B). Compared to the C group, VP intervention can downregulate 1004 DEGs (C) and upregulate 540 DEGs (D), restoring them to baseline levels.

Differential gene expression analysis across the control (C), UVB-exposed model (M), and VP-treated (VP) groups revealed substantial transcriptomic changes. UVB exposure induced 10,841 differentially expressed genes (DEGs) relative to the control, with 5467 upregulated and 5374 downregulated. Importantly, VP treatment modulated 4284 genes compared to the model group, among which 1544 genes (540 upregulated, 1004 downregulated) exhibited a reversal of expression toward baseline levels (Fig. 6). These results indicate that VP mitigates UVB-induced photodamage by normalizing the expression of a broad set of genes, collectively representing potential key mediators of its protective activity.

3.5.2. *The key pathways of the protection against UVB-induced skin photodamage*

To elucidate the functional mechanisms of VP, Gene Ontology (GO) enrichment analysis was conducted across three categories: Biological Process, Cellular Component, and Molecular Function. The results revealed that VP influenced processes including cellular metabolism, signal transduction, and response to stimuli; involved cellular structures such as intracellular components and protein complexes; and affected molecular functions like binding, catalytic activity, and transporter activity. These findings collectively outline the multidimensional biological roles of VP in mitigating UVB-induced skin injury. KEGG pathway analysis further demonstrated that differentially expressed genes (DEGs) were significantly enriched in several key pathways associated with UVB-induced photodamage (Fig. 7). These included apoptosis, PI3K-Akt, NF-κB, MAPK, TNF, and cytokine-cytokine receptor interaction pathways, among others. Previous studies have established that UV irradiation triggers dysregulated apoptosis and inflammatory responses through aberrant activation of MAPK, NF-κB, and PI3K-Akt signaling, as well as disruption of the mTOR-autophagy axis. Our data thus suggest that VP may ameliorate UVB-induced damage by modulating pathways critical to apoptosis, inflammation, and immune regulation.

3.5.3. *Interaction network of intersecting target genes*

To elucidate the molecular network underlying the photoprotective effects of VP, we constructed a protein-protein interaction network using differentially expressed genes identified from key pathways, including the PI3K-Akt, NOD-like receptor, cytokine-cytokine receptor, TNF, and mTOR signaling pathways. The network was generated *via* the STRING database and visualized (Fig. 8A). Analysis revealed several hub genes

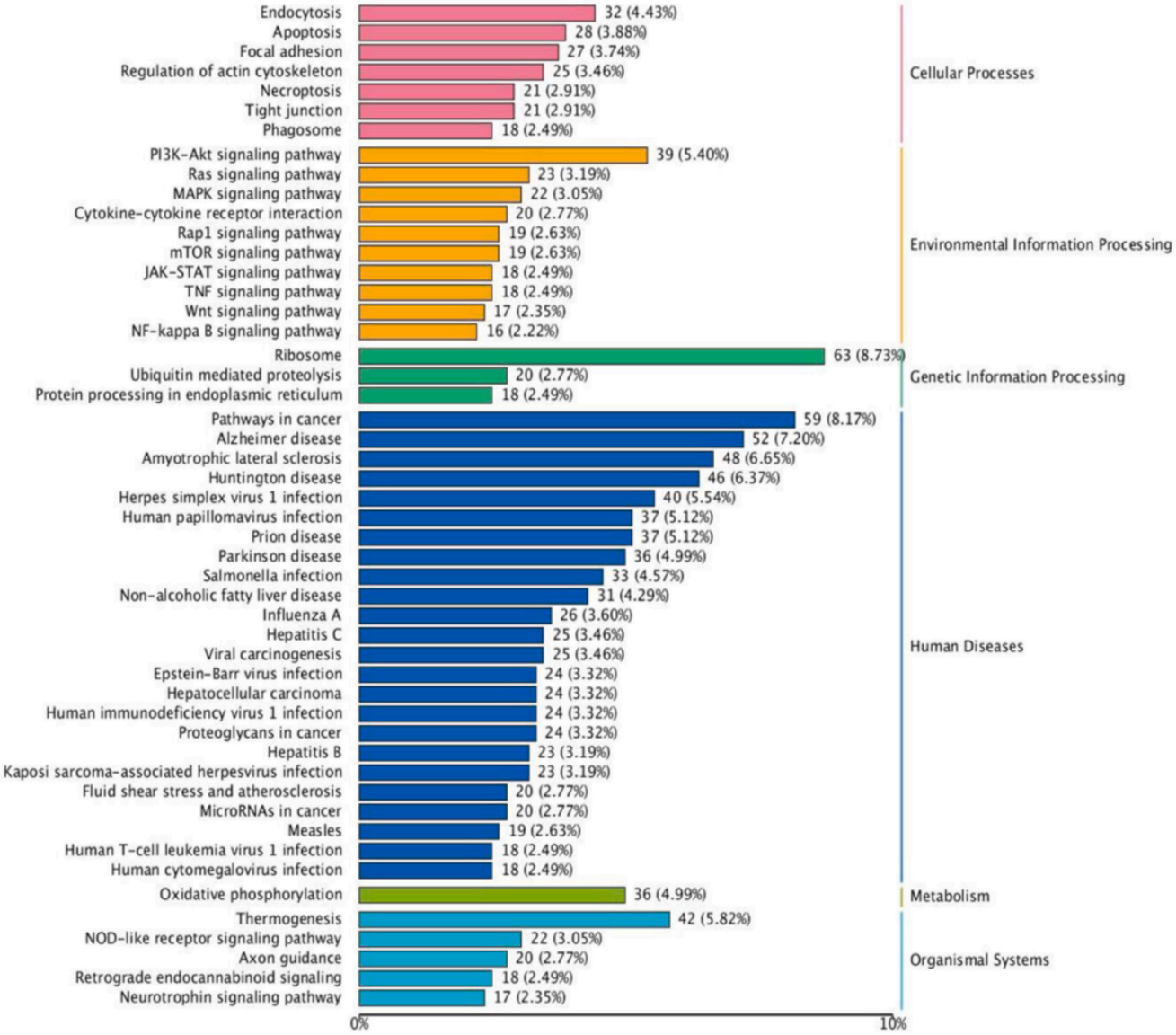

Fig. 7. The KEGG annotation and enrichment of action was analyzed.

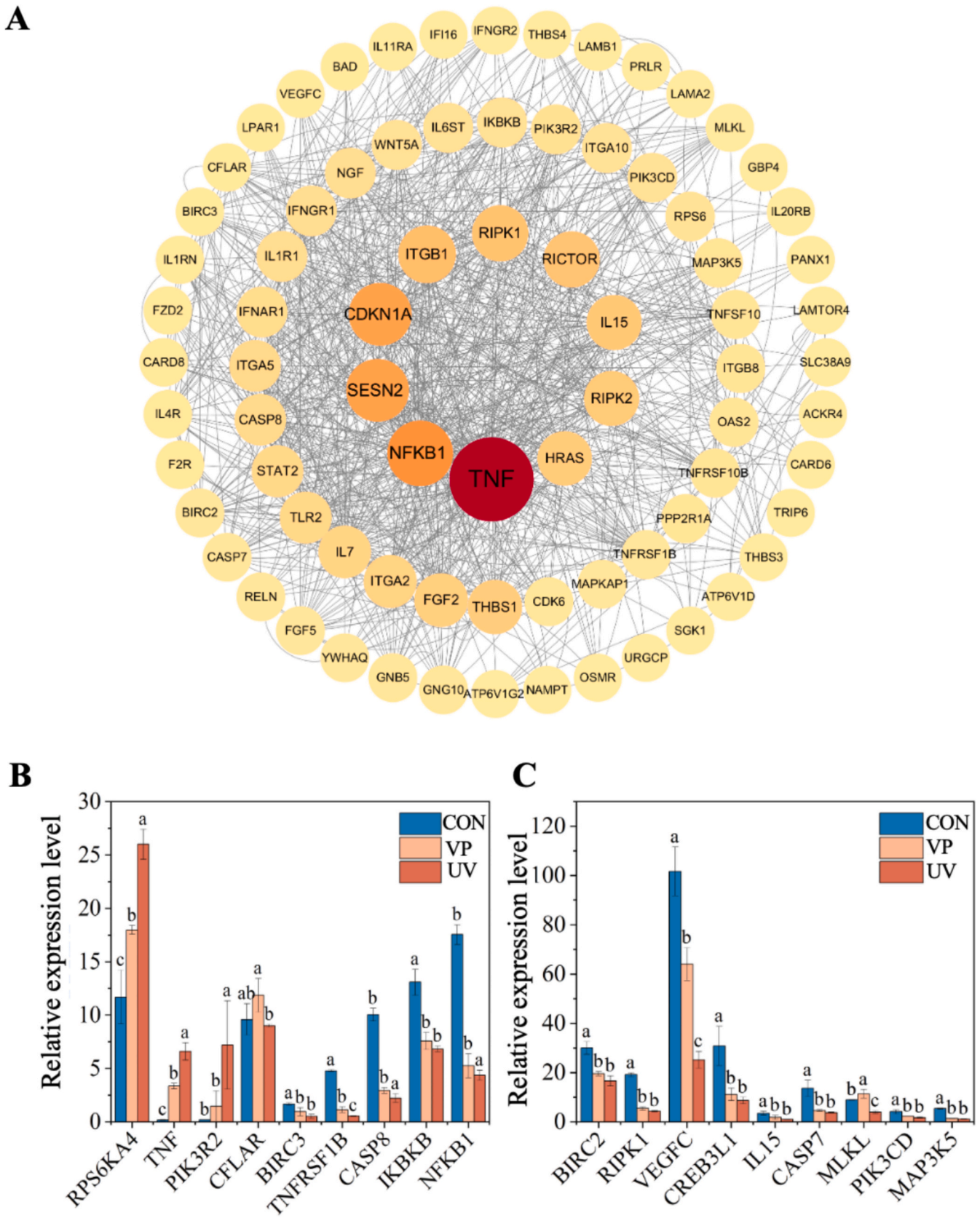

Fig. 8. TNF pathway was the key to VP exerting the protective effects of skin photoaging. (A) PPI network of key differentially expressed genes. (B, C) Differential gene expression levels involved in the TNF pathway. All values are presented as means ± SD ($n = 3$), it is statistical significance between different letters.

with high connectivity, such as TNF and NFKB1 (nuclear factor kappa B subunit 1), indicating their central regulatory roles in the VP-mediated response to UVB-induced skin injury. These findings align with prior KEGG enrichment results and existing literature, where NFKB1 is recognized as a key regulator of NF-κB activity. Notably, TNF displayed the highest node degree within the network, reflecting its pivotal position in a signaling cascade that modulates inflammation, apoptosis, and immune responses—processes known to be critically involved in UV-induced skin damage [75]. As illustrated in Fig. 8B and C, UVB exposure (model group) significantly upregulated the expression of TNF, RPS6KA4, and PIK3R2 compared to the control, while VP treatment effectively counteracted these changes. Moreover, VP significantly upregulated a panel of UVB-induced genes involved in TNF signaling, such as VEGFC, MLKL. These validation outcomes are consistent with the RNA-seq data, thereby reinforcing the credibility of our transcriptomic analysis. A schematic representation of the regulatory impact of VP on the TNF pathway is provided in Fig. 9. In summary, these results indicate that VP mitigates UVB-induced skin photoaging through multi-target mechanisms, with the TNF signaling pathway serving as a central hub for its bioactivity.

4. Conclusion

This study presents a systematic comparison of the physicochemical properties and bioactivities of polysaccharides extracted from various parts of *D. rubrovalvata*, with particular focus on the underutilized volva colloid in contrast to the edible stipe and pileus. IP, FP and VP demonstrated protective effects against UVB-induced damage in HSF cells, as evidenced by the restoration of antioxidant enzyme activities and reduction in oxidative stress markers. Among them, VP displayed the most potent photoprotective capacity. Mechanistic investigation further revealed that VP alleviates UVB-induced skin photodamage primarily by modulating key cellular processes including apoptosis, inflammation, and immune response. The TNF signaling pathway was identified as a central mechanism through which VP exerts its repair effects. However, this study was conducted solely using *in vitro* cellular models, and therefore, the anti-photoaging effects of VP, IP, and FP have not yet been validated in animal or human skin models, which limits the direct translatability of our findings to clinical or real-world applications. Additionally, a more detailed structural elucidation, such as glycosidic linkage patterns, degree of branching, and fine chain conformation, remains to be performed, which would be essential for fully understanding the structure-activity relationships underlying their bioactivities. In conclusion, the distinctive structural features and compelling bioactivities of VP underscore its potential as a valuable functional material, providing a scientific foundation for the high-value utilization of discarded *D. rubrovalvata* volva.

CRediT authorship contribution statement

Ziwei Li: Writing – original draft, Data curation. **Peng Liu:** Writing – original draft, Methodology. **Di Wu:** Methodology, Formal analysis. **Zhong Zhang:** Supervision, Formal analysis. **Wanchao Chen:** Investigation, Data curation. **Wen Li:** Supervision, Investigation. **Yuanfeng Wang:** Supervision, Project administration. **Yan Yang:** Writing – review & editing, Project administration.

Declaration of competing interest

The authors declare that they have no known competing financial

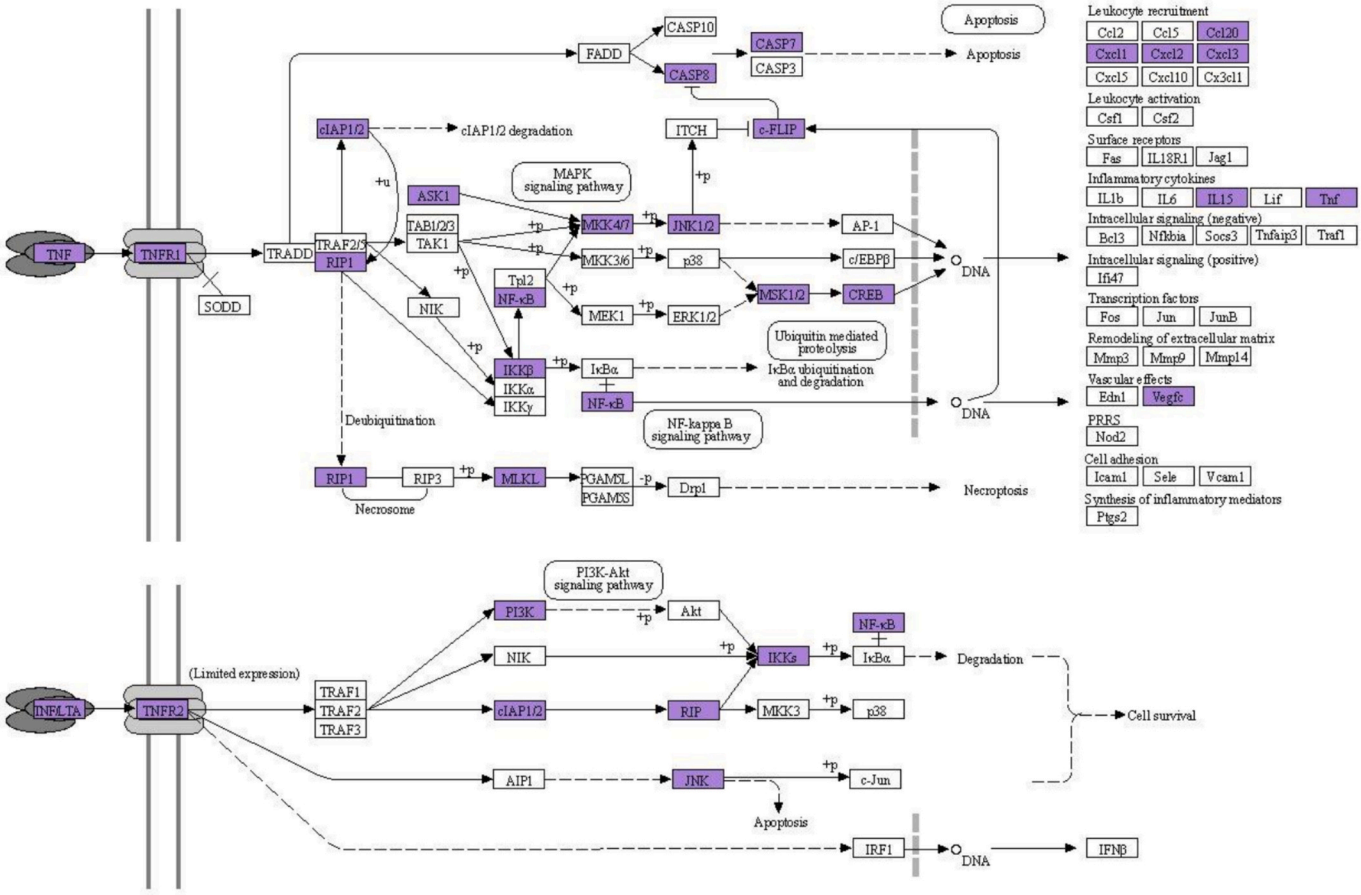

Fig. 9. Visualization of key genes in the TNF pathway regulated by VP. The genes marked in purple were significantly regulated by VP.

interests or personal relationships that could have appeared to influence the work.

Acknowledgments

This work was supported by the “Zhupao” Program of Shanghai Academy of Agricultural Sciences (ZP25161).

Data availability

Data will be made available on request.

References

[1] K.J. Gromkowska-Kepka, A. Puscion-Jakubik, R. Markiewicz-Zukowska, K. Socha, The impact of ultraviolet radiation on skin photoaging - review of in vitro studies, J. Cosmet. Dermatol. 20 (11) (2021) 3427–3431.
[2] A. Hajialiasgary Najafabadi, M.H. Soheilifar, N. Masoudi-Khoram, Exosomes in skin photoaging: biological functions and therapeutic opportunity, Cell Commun. Signal 22 (1) (2024) 32.
[3] G.J. Fisher, S. Kang, J. Varani, Z. Bata-Csorgo, Y. Wan, S. Datta, J.J. Voorhees, Mechanisms of photoaging and chronological skin aging, Arch. Dermatol. 138 (11) (2002) 1462–1470.
[4] M. Liu, F. Lu, J. Feng, Therapeutic potential of aIPose tissue derivatives in skin photoaging, Regen. Med. 18 (11) (2023) 869–883.
[5] K.J. Gromkowska-Kępka, A. Puścion-Jakubik, R. Markiewicz-Żukowska, K. Socha, The impact of ultraviolet radiation on skin photoaging - review of in vitro studies, J. Cosmet. Dermatol. 20 (11) (2021) 3427–3431.
[6] G. Petruk, G.R. Del, M.M. Rigano, D.M. Monti, Antioxidants from plants protect against skin photoaging, Oxidative Med. Cell. Longev. 2018 (2018) 1454936.
[7] K. Scharffetter-Kochanek, P. Brenneisen, J. Wenk, G. Herrmann, W. Ma, L. Kuhr, C. Meewes, M. Wlaschek, Photoaging of the skin from phenotype to mechanisms, Exp. Gerontol. 35 (3) (2000) 307–316.
[8] Y. Xia, H. Zhang, X. Wu, Y. Xu, Q. Tan, Resveratrol activates autophagy and protects from uva-induced photoaging in human skin fibroblasts and the skin of male mice by regulating the ampk pathway, Biogerontology 25 (4) (2024) 649–664.
[9] J. Sun, Y. Jiang, J. Fu, L. He, X. Guo, H. Ye, C. Yin, H. Li, H. Jiang, Beneficial effects of epigallocatechin gallate in preventing skin photoaging: a review, Molecules 29 (22) (2024).
[10] X. Zhang, H. Zhuang, S. Wu, C. Mao, Y. Dai, H. Yan, Marine bioactive peptides: anti-photoaging mechanisms and potential skin protective effects, Curr. Issues Mol. Biol. 46 (2) (2024) 990–1009.
[11] R. Pangestuti, K.H. Shin, S.K. Kim, Anti-photoaging and potential skin health benefits of seaweeds, Mar. Drugs 19 (3) (2021).
[12] L. Guo, Y. Yang, Y. Pu, S. Mao, Y. Nie, Y. Liu, X. Jiang, Dendrobium officinale kimura & migo polysaccharide and its multilayer emulsion protect skin photoaging, J. Ethnopharmacol. 318 (Pt B) (2024) 116974.
[13] J. Lin, Y.Y. Lu, H.Y. Shi, P. Lin, Chaga medicinal mushroom, inonotus obliquus (agaricomycetes), polysaccharides alleviate photoaging by regulating nrf2 pathway and autophagy, Int. J. Med. Mushrooms 25 (10) (2023) 49–64.
[14] T. Li, X. Cheng, K. Bao, L. Wang, M. Song, J. Wang, S. Wang, S. Wang, T. Wen, H. Sun, Z. Zhu, Structural characterization, antioxidant activity, and mechanism of polysaccharides isolated from Dictyophora rubrovalvata stipet, Int. J. Biol. Macromol. 306 (Pt 3) (2025) 141576.
[15] Y. Jiang, J. An, Y. Xia, Q. Fei, D. Wang, Y. Lu, W. Wu, Design, synthesis, and antimicrobial evaluation of novel 1,2,4-trizaole thioether derivatives with a 1,3,4-thiadiazole skeleton, RSC Adv. 5 (34) (2025) 28084–28092.
[16] X. Du, J. Wang, L. Gao, J. Zheng, L. Zhang, Study on the structural characterization and biological activities of polysaccharides from *Dictyophora rubrovolvata* and its silver nanoparticles, Int. J. Biol. Macromol. 28 (Pt 1) (2025) 147632.
[17] M. Song, J. Wang, K. Bao, C. Sun, X. Cheng, T. Li, S. Wang, S. Wang, T. Wen, Z. Zhu, Isolation, structural characterization and immunomodulatory activity on RAW264.7 cells of a novel exopolysaccharide of Dictyophora rubrovalvata, Int. J. Biol. Macromol. 270 (Pt 2) (2024) 132222.
[18] N. Huang, Y.N. Yang, J. Huang, H.Y. Shao, Y.L. Li, S.H. Qin, H.F. Li, X.J. Shen, L. Yang, J.M. Hu, Structure characterization and immunoactivity on dendritic cells of two neutral polysaccharides from Dictyophora rubrovalvata, Nat Prod Bioprospect. 14 (1) (2024) 52.
[20] D. Michel, A.G. K, K.H. J, A.R. P, S. Fred, Colorimetric method for determination of sugars and related substances, Anal. Chem. 28 (3) (1956).
[21] N. Blumenkrantz, G. Asboe-Hansen, New method for quantitative determination of uronic acids, Anal. Biochem. 54 (2) (1973).
[22] X. Du, Y. Zhang, H. Mu, Z. Lv, Y. Yang, J. Zhang, Structural elucidation and antioxidant activity of a novel polysaccharide (tapb1) from tremella aurantialba, Food Hydrocoll. 43 (2015) 459–464.
[23] T. Li, Y. Yang, Y. Liu, S. Zhou, M.Q. Yan, D. Wu, J. Zhang, C. Tang, Physicochemical characteristics and biological activities of polysaccharide fractions from phellinus baumii cultured with different methods, Int. J. Biol. Macromol. 81 (2015) 1082–1088.
[24] T. Li, L. Chen, D. Wu, G. Dong, W. Chen, H. Zhang, Y. Yang, W. Wu, The structural characteristics and biological activities of intracellular polysaccharide derived from mutagenic sanghuangporous sanghuang strain, Molecules 25 (16) (2020) 3693.
[25] J. Yan, Z. Ding, X. Gao, Y. Wang, Y. Yang, D. Wu, H. Zhang, Comparative study of physicochemical properties and bioactivity of hericium erinaceus polysaccharides at different solvent extractions, Carbohydr. Polym. 193 (2018) 373–382.
[26] M.D. Mtetwa, L. Qian, H. Zhu, F. Cui, X. Zan, W. Sun, D. Wu, Y. Yang, Ultrasound-assisted extraction and antioxidant activity of polysaccharides from acanthus ilicifolius, J. Food Meas. Charact. 14 (3) (2020) 1223–1235.
[27] M. Shi, Z. Zhang, Y. Yang, Antioxidant and immunoregulatory activity of ganoderma lucidum polysaccharide (glp), Carbohydr. Polym. 95 (1) (2013) 200–206.
[28] Y. Wang, J. Yin, X. Huang, S. Nie, Structural characteristics and rheological properties of high viscous glucan from fruit body of dictyophora rubrovolvata, Food Hydrocoll. 101 (2020) 105514.
[29] Y. Dong, T. Lan, Z. Liu, Z. Xu, L. Jiang, Y. Zhang, X. Sui, Shear, extensional rheology, and tribology of polysaccharide-thickened soy protein-based liquid systems for dysphagia management, Food Chem. 463 (Pt 1) (2025) 141145.
[30] X. Pan, X. Chen, H. Niu, M. Shen, X. Ye, S. Mo, J. Xie, Large and small amplitude oscillatory shear techniques evaluate the nonlinear rheological properties of ficus pumila polysaccharide -wheat starch gel, Int. J. Biol. Macromol. 270 (Pt 1) (2024) 132352.
[31] R. Barbucci, D. Pasqui, R. Favaloro, G. Panariello, A thixotropic hydrogel from chemically cross-linked guar gum: synthesis, characterization and rheological behaviour, Carbohydr. Res. 343 (18) (2008) 3058–3065.
[32] X. Shi, W. Cheng, Q. Wang, J. Zhang, C. Wang, M. Li, D. Zhao, D. Wang, Q. An, Exploring the protective and reparative mechanisms of g. Lucidum polysaccharides against h2o2-induced oxidative stress in human skin fibroblasts, Clin. Cosmet. Investig. Dermatol. 14 (2021) 1481–1496.
[33] H. Chen, C. Lin, Y. Wu, B. Wang, M. Kui, J. Xu, H. Ma, J. Li, J. Zeng, W. Gao, K. Chen, Protective effects of degraded bletilla striata polysaccharides against uvb-induced oxidative stress in skin, Int. J. Biol. Macromol. 277 (Pt 3) (2024) 134462.
[34] L. Fan, X. Luan, Y. Jia, L. Ma, Z. Wang, Y. Yang, Q. Chen, X. Cui, D. Luo, Protective effect and mechanism of lycium barbarum polysaccharide against uvb-induced skin photoaging, Photochem. Photobiol. Sci. 23 (10) (2024) 1931–1943.
[35] H. Zhang, Y. Liu, B. Yu, R. Lu, An optimized trizol-based method for isolating rna from adipose tissue, Biotechniques 74 (5) (2023) 203–209.
[36] L. Zhang, X. Ye, T. Ding, X. Sun, Y. Xu, D. Liu, Ultrasound effects on the degradation kinetics, structure and rheological properties of apple pectin, Ultrason. Sonochem. 20 (1) (2013) 222–231.
[37] X. Bai, X. Bai, Antioxidant activity of a polysaccharide from dictyophora indusiata volva and mecc analysis of its monosaccharide composition, J. Indian Chem. Soc. 98 (10) (2021) 100146.
[38] Y. Hua, B. Yang, J. Tang, Z. Ma, Q. Gao, M. Zhao, Structural analysis of water-soluble polysaccharides in the fruiting body of dictyophora indusiata and their in vivo antioxidant activities, Carbohydr. Polym. 87 (1) (2012) 343–347.
[39] A.O. Aremu, N.A. Masondo, Z. Molnár, W.A. Stirk, V. ördög, J. Van Staden, Changes in phytochemical content and pharmacological activities of three *Chlorella* strains grown in different nitrogen conditions, J. Appl. Phycol. 28 (1) (2016) 149–159.
[40] W. Wang, X. Song, Z. Gao, H. Zhao, X. Wang, M. Liu, L. Jia, Anti-hyperlipidemic, antioxidant and organic protection effects of acidic-extractable polysaccharides from dictyophora indusiata, Int. J. Biol. Macromol. 129 (2019) 281–292.
[41] Q. Li, J. Li, H. Li, R. Xu, Y. Yuan, J. Cao, Physicochemical properties and functional bioactivities of different bonding state polysaccharides extracted from tomato fruit, Carbohydr. Polym. 219 (2019) 181–190.
[42] G. Ma, W. Yang, A.M. Mariga, Y. Fang, N. Ma, F. Pei, Q. Hu, Purification, characterization and antitumor activity of polysaccharides from pleurotus eryngii residue, Carbohydr. Polym. 114 (2014) 297–305.
[43] M. Al-Kelani, N. Buthelezi, Advancements in medical research: exploring Fourier transform infrared (ftir) spectroscopy for tissue, cell, and hair sample analysis, Skin Res. Technol. 30 (6) (2024) e13733.
[44] B. Gieroba, G. Kalisz, M. Krysa, M. Khalavka, A. Przekora, Application of vibrational spectroscopic techniques in the study of the natural polysaccharides and their cross-linking process, Int. J. Mol. Sci. 24 (3) (2023) 2630.
[45] J. Xu, Z. Chen, P. Liu, Y. Wei, M. Zhang, X. Huang, L. Peng, X. Wei, Structural characterization of a pure polysaccharide from bletilla striata tubers and its protective effect against h2o2-induced injury fibroblast cells, Int. J. Biol. Macromol. 193 (2021) 2281–2289.
[46] X. Hu, F. Xu, J. Li, J. Li, C. Mo, M. Zhao, L. Wang, Ultrasonic-assisted extraction of polysaccharides from coix seeds: optimization, purification, and in vitro digestibility, Food Chem. 374 (2022) 131636.
[48] Z. Zamani, S.M.A. Razavi, Physicochemical, rheological and functional properties of nettle seed (urtica pilulifera) gum, Food Hydrocoll. 112 (2021) 106304.
[49] F. Huang, Y. Liu, R. Zhang, L. Dong, Y. Yi, Y. Deng, Z. Wei, G. Wang, M. Zhang, Chemical and rheological properties of polysaccharides from litchi pulp, Int. J. Biol. Macromol. 112 (2018) 968–975.
[50] K. Arab, B. Ghanbarzadeh, S. Karimi, B. Ebrahimi, M. Hosseini, Gelling and rheological properties of a polysaccharide extracted from ocimum album l. seed, Int. J. Biol. Macromol. 246 (2023) 125603.
[51] W. Xiao, M. Shen, Y. Ren, H. Wen, J. Li, L. Rong, W. Liu, J. Xie, Controlling the pasting, rheological, gel, and structural properties of corn starch by incorporation of debranched waxy corn starch, Food Hydrocoll. 123 (2022) 107136.
[52] W. Cai, T. Hu, Q. Huang, Rheological properties and critical concentrations of a hyperbranched polysaccharide from lignosus rhinocerotis sclerotia, Int. J. Biol. Macromol. 202 (2022) 46–54.

[53] P. Zhou, M. Eid, W. Xiong, C. Ren, T. Ai, Z. Deng, J. Li, B. Li, Comparative study between cold and hot water extracted polysaccharides from plantago ovata seed husk by using rheological methods, Food Hydrocoll. 101 (2020) 105465.
[54] Y.P. Timilsena, R. Adhikari, S. Kasapis, B. Adhikari, Rheological and microstructural properties of the chia seed polysaccharide, Int. J. Biol. Macromol. 81 (2015) 991–999.
[55] A.C.F. de Brito, M.R. Sierakowski, F. Reicher, J.P.A. Feitosa, R.C.M. de Paula, Dynamic rheological study of sterculia striata and karaya polysaccharides in aqueous solution, Food Hydrocoll. 19 (5) (2005) 861–867.
[56] L. Rivera-Hernández, N. Chavarría-Hernández, A. Tecante, M.A. López-Ortega, M. D.R. López Cuellar, A. Rodríguez-Hernández, Mixed gels based on low acyl gellan and citrus pectin: a linear viscoelastic analysis, Food Hydrocoll. 137 (2023) 108353.
[57] L.L. Hyland, M.B. Taraban, Y. Feng, B. Hammouda, Y.B. Yu, Viscoelastic properties and nanoscale structures of composite oligopeptide-polysaccharide hydrogels, Biopolymers 97 (3) (2012) 177–188.
[58] L. Bai, P. Zhu, W. Wang, M. Wang, The influence of extraction ph on the chemical compositions, macromolecular characteristics, and rheological properties of polysaccharide: the case of okra polysaccharide, Food Hydrocoll. 102 (2020) 105586.
[59] F. Hentati, G. Pierre, A.V. Ursu, C. Vial, C. Delattre, S. Abdelkafi, P. Michaud, Rheological investigations of water-soluble polysaccharides from the tunisian brown seaweed cystoseira compressa, Food Hydrocoll. 103 (2020) 105631.
[60] L. Qiao, Y. Li, Y. Chi, Y. Ji, Y. Gao, H. Hwang, W.G. Aker, P. Wang, Rheological properties, gelling behavior and texture characteristics of polysaccharide from enteromorpha prolifera, Carbohydr. Polym. 136 (2016) 1307–1314.
[61] M. Miao, A. Bai, B. Jiang, Y. Song, S.W. Cui, T. Zhang, Characterisation of a novel water-soluble polysaccharide from leuconostoc citreum sk24.002, Food Hydrocoll. 36 (2014) 265–272.
[62] J. Montoya, J. Medina, A. Molina, J. Gutiérrez, B. Rodríguez, R. Marín, Impact of viscoelastic and structural properties from starch-mango and starch-arabinoxylans hydrocolloids in 3d food printing, Addit. Manuf. 39 (2021) 101891.
[63] A. Salminen, K. Kaarniranta, A. Kauppinen, Photoaging: uv radiation-induced inflammation and immunosuppression accelerate the aging process in the skin, Inflamm. Res. 71 (7–8) (2022) 817–831.
[64] X. Chen, C. Yang, G. Jiang, Research progress on skin photoaging and oxidative stress, Postep. Dermatol. Alergol. 38 (6) (2021) 931–936.
[65] Y. Zhang, B. Sun, L. Wang, W. Shen, S. Shen, X. Cheng, X. Liu, H. Xia, Curcumin-loaded liposomes in gel protect the skin of mice against oxidative stress from photodamage induced by uv irradiation, Gels 10 (9) (2024).
[66] W.Y. Quan, L.H. Fan, Q. Li, C.M. Lin, Y.Y. Liang, Q. Zhang, H. Ye, X.J. Li, K.F. Wu, Y.Z. Zhu, Dhpw1 attenuation of uvb-induced skin photodamage in human immortalized keratinocytes, Exp. Gerontol. 166 (2022) 111897.
[67] H. Fu, S. You, D. Zhao, Q. An, J. Zhang, C. Wang, D. Wang, M. Li, Tremella fuciformis polysaccharides inhibit uva-induced photodamage of human dermal fibroblast cells by activating up-regulating nrf2/keap1 pathways, J. Cosmet. Dermatol. 20 (12) (2021) 4052–4059.
[68] L. Wang, K. Yang, R. Jing, W. Zhao, K. Guo, Z. Hu, G. Liu, N. Xu, J. Zhao, L. Lin, S. Gao, Protective effect of saussurea involucrata polysaccharide against skin dryness induced by ultraviolet radiation, Front. Pharmacol. 14 (2023) 1089537.
[69] Y.I. Kim, W.S. Oh, P.H. Song, S. Yun, Y.S. Kwon, Y.J. Lee, S.K. Ku, C.H. Song, T. H. Oh, Anti-photoaging effects of low molecular-weight fucoidan on ultraviolet b-irradiated mice, Mar. Drugs 16 (8) (2018).
[70] M. De Tollenaere, M. Meunier, L. Lapierre, E. Chapuis, A. Guilleret, I. Harrison, T. Jean, A. Rannou, A. Scandolera, R. Reynaud, High molecular weight hyaluronic acid vectorised with clay provides long-term hydration and reduces skin brightness, Skin Res. Technol. 30 (4) (2024) e13672.
[71] Q. Guo, F. Li, Y. Duan, C. Wen, W. Wang, L. Zhang, R. Huang, Y. Yin, Oxidative stress, nutritional antioxidants and beyond, Sci. China Life Sci. 63 (6) (2020) 866–874.
[72] A. Zhang, Y. Shen, M. Cen, X. Hong, Q. Shao, Y. Chen, B. Zheng, Polysaccharide and crocin contents, and antioxidant activity of saffron from different origins, Ind. Crop. Prod. 133 (2019) 111–117.
[73] T.C. Lo, C.A. Chang, K. Chiu, P. Tsay, J. Jen, Correlation evaluation of antioxidant properties on the monosaccharide components and glycosyl linkages of polysaccharide with different measuring methods, Carbohydr. Polym. 86 (1) (2011) 320–327.
[74] Z. Wang, J. Xie, M. Shen, S. Nie, M. Xie, Sulfated modification of polysaccharides: synthesis, characterization and bioactivities, Trends Food Sci. Technol. 74 (2018) 147–157.
[75] M. Tjioe, M.J. Gerritsen, A.A. Den Broeder, C.A. Van Hooijdonk, E.J. Kroot, P. L. Van Riel, P. Barrera, P.C. Van De Kerkhof, Adalimumab, a fully human anti-tnf-alpha monoclonal antibody, treatment does not influence experimental uv response in the skin of rheumatoid arthritis patients, Exp. Dermatol. 12 (4) (2003) 460–465.